Measurement-based Wideband Radio Channel Characterization in an Underground Parking Lot

Yang Miao, Wei Wang, José Rodríguez-Piñeiro, Tomás Domínguez-Bolaño, Yi Gong

Abstract—This paper reports the wideband radio channel measurement and characterization in an underground parking lot at frequency band from 4.9 GHz to 5.9 GHz. Single-input single-output and virtual single-input multiple-output channels are measured point-to-point by the Vector Network Analyzer based system. The measurements include both obstructed line-of-sight and non-line-of-sight scenarios, include influences of not only vehicles but also pillars which are commonly seen in underground parking. The radio channel modeling parameters, including path loss, delay spread, coherence bandwidth, power delay profile, reverberation time and power angular delay profile are summarized and analyzed. It is interesting to observe that due to the existence of objects like vehicles, pillars, and ceiling, the radio channels measured in underground parking presents rich spatial diversity even within a small area less than 50 **m**^{2}.

Index Terms—Radio propagation channel, wideband, underground parking

I. Introduction

The radio wave propagation in underground garage is a unique, common and important scenario for the future wireless-enabled intelligent transportation in urban or suburban regions. Different from offices, residences, or aboveground open garages, the underground garages are more like a closed cavity with presences of vehicles, supporting pillars, ventilation ducts, or rotary tunnels connecting different floors. The underground environment is normally GPS-denied, therefore the desired functions, for instance the localization in the application of autonomous parking, are more likely to be enabled by local wireless radio networks. Hence the studies on the radio channel in underground garages are called for.

The radio channels with ultra-wide bandwidth can provide high resolution in time domain, and have been considered as a feasible solution for indoor applications like localization [1]. However, the wideband channel in underground parking garage has not yet been fully investigated. In [2], the measurement-based radio channel characterizations from 3.28 GHz to 5.04 GHz in an underground garage have been reported. All measurements are implemented with clear line-of-sight (LOS) and the geometrical complexity for radio wave propagation is low. There is no study on the non-LOS (NLOS) or the transition between LOS and NLOS scenarios, which may occur with high probability in real-world applications. In [3], the wideband radio propagation out-of-vehicle in an underground garage from 3 GHz to 11 GHz has been reported, for the purpose of localizing nearby vehicles in LOS scenario. The main focus is the interaction between radio waves and the vehicle without much consideration of the background objects in the garage.

In this paper, the wideband radio channel measurements in an underground parking lot considering both obstructed LOS and NLOS scenarios, both the radio interaction with vehicle and background objects are reported. The measured channels are with single input and virtual multiple output (virtual SIMO), or with single input and single output (SISO), and are characterized both in time and angular domains. Similarly as in [2], [3], mobility is not considered in our measurements due to the constraints of Vector Network Analyzer (VNA) based system. Nevertheless, the analyzed point-to-point scenarios well expand the cognition of the underground parking radio communications. The rest of this paper is as follows. Section II reports the measurement campaign, Section III reports the channel characterizations, and Section IV concludes this paper.

II. Measurement Campaign

Measurements were performed in the underground garage of Faculty Research Building in Southern University of Science and Technology, Shenzhen, China. Two ports of Keysight N5227A-419 PNA Microwave Network Analyzer were connected to two Ettus VERT 2450 dipole antennas by 12-meter long cables. The VERT 2450 dipole is vertically polarized omnidirectional antenna with 3dBi gain. At the transmit antenna (Tx) side, one dipole connecting to PNA port 1 was mounted on a tripod; at the receive antenna (Rx) side, one dipole connecting to PNA port 2 was mounted on another tripod, and this dipole can be translational moved along a circle whose radius is 4.5 cm. The virtual SIMO channel was measured by moving Rx along the circle for $360°$ degrees with angular step of $30°$, and the calibrated S_{21} data was recorded. The dimension of virtual SIMO channel transfer function (CTF) $\boldsymbol{H}$ is 12×1 for one frequency point. It is assumed that the propagation environment stays static during the movement of Rx. The frequency range was set to 4.9 GHz - 5.9 GHz with 1 GHz span. In addition, a few SISO measurements were also conducted. The PNA swept linearly in the frequency range with totally 1601 points, and it took about 11.6 ms for one sweep. For each measurement, we swept totally about 50 times.

Fig. 1 shows the schematic graph of the measurement environment, and Table I shows the measured scenarios. Note that only the vehicles and pillars in the vicinity of the Tx and Rx are shown in the figure; the underground parking has a large volume and a lot of pillars and cars parked elsewhere. During the measurement, the heights of Tx and Rx were fixed to 1.46 m, and the distance from Tx (or Rx) to the ceiling was 2.8 m. The heights of car 1 and car 2 are about 1.5 m.
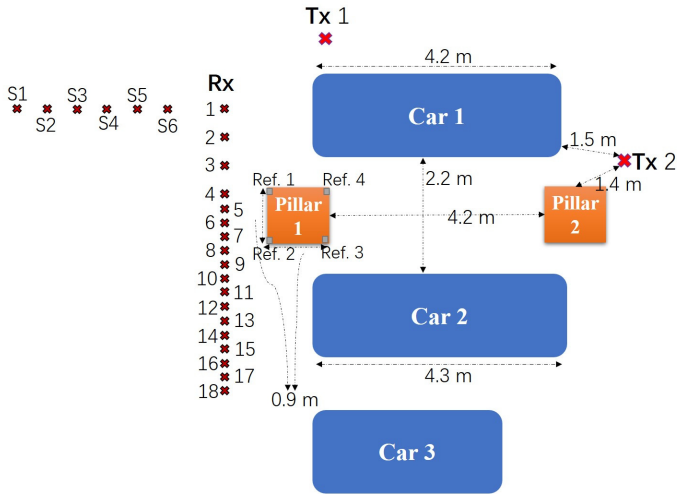
Fig. 1. Schematic graph of measurement environment (the object distance in the figure is not proportional to the actual object distance)

TABLE I
MEASUREMENT SCENARIOS

Index	Tx loc.	Rx loc.		PL [dB]	T_{rev} [ns]	DS [ns]	CB [MHz]
1		1	LOS	54.02	31.97	10.60	28.75
2		2	LOS	56.53	34.09	13.45	10.00
3		3	LOS	57.08	33.85	13.94	7.50
4		4	LOS	58.95	33.50	16.05	5.63
5		5	LOS	58.41	34.34	14.11	7.50
6		6	LOS	58.66	35.64	14.53	6.88
7		7	LOS	59.71	38.68	15.70	6.88
8	1	8	SIMO LOS	59.80	37.58	15.33	6.88
9		9	LOS	62.38	36.40	19.45	3.75
10		10	LOS	63.44	42.75	21.82	3.13
11		11	LOS	66.15	42.65	27.05	2.50
12		12	NLOS	68.10	38.98	26.83	2.50
13		13	NLOS	69.00	33.62	26.30	2.50
14		14	NLOS	69.80	32.92	27.11	1.88
15		16	NLOS	70.65	31.12	27.11	1.88
16		18	NLOS	71.47	30.79	27.97	1.88
17		17	LOS	71.23	39.37	27.78	1.88
18	2	18	NLOS	70.06	42.88	25.40	2.50
19		3	SIMO LOS	73.03	28.08	15.33	4.38
20		1	NLOS	67.68	33.98	18.99	3.75
21		S1	NLOS	80.89	77.46	29.79	1.88
22		S2	LOS	77.88	45.69	26.18	2.50
23	2	S3	SISO LOS	77.38	65.20	25.05	2.50
24		S4	LOS	76.50	59.16	25.63	2.50
25		S5	NLOS	76.32	44.75	26.73	1.88
26		S6	NLOS	72.62	42.11	20.10	3.13

When there is direct line between Tx and Rx (laser rangefinder is used here), their distance is recorded and this scenario is marked as obstructed LOS; when there is no direct line between Tx and Rx, the distances between the Rx and the visible reference points $1-4$ on the corners of pillar 1 are recorded, and this scenario is marked as NLOS. In addition to the virtual SIMO measurements (scenario $1 \sim 20$), there are some SISO measurements (scenario $21 \sim 26$) for the purpose of checking the shadowing/scattering effect due to car 1.

III. CHANNEL CHARACTERIZATION

A. Power Delay Profile

The temporal domain channel is characterized by power delay profile (PDP) given by

$$\text{PDP} = \frac{1}{N_{\text{R}} N_{\text{T}}} \sum_{n_{\text{r}}=1}^{N_{\text{R}}} \sum_{n_{\text{t}}=1}^{N_{\text{T}}} |\text{IFFT}\{\text{HannWindow}\{H_{n_{\text{r}} n_{\text{t}}}\}\}|^2 \quad (1)$$

where $H_{n_{\text{r}} n_{\text{t}}}$ denotes the CTF of the n_{t}-th Tx and the n_{r}-th Rx. N_{R} and N_{T} are the total numbers of Rx and Tx at each measurement point, respectively. For calculating the PDP of SISO channel, both N_{R} and N_{T} are 1. For calculating the PDP of virtual SIMO channel, N_{T} is 1 and N_{R} is 12. Hann window is used to suppress the side lobe. Averaging of PDP over snapshots further reduces the noise floor and the effect of the noise over the PDP estimation. Fig. 2 (a) shows the examples of PDP of the measured scenarios. It can be seen that the noise floor of the obstructed LOS scenarios (about -111 dB) is clearly higher than that for the NLOS scenarios (about -116 dB). In fact, this noise floor is effect both by the inverse Fourier transform and the signal-to-noise (SNR) ratio, and is not the absolute noise variance. The SNR for the obstructed LOS scenario is larger than that of the NLOS scenario; for a fixed dynamic range, the noise floor for the obstructed LOS scenario can not be decreased more than that of the NLOS scenario by the gain of inverse Fourier transform. In addition,

there is a clear trend that the first peak of PDP comes at later time with the increase of the distance between Tx and Rx as well as the occurrence of the obstruction of pillar 1.

Moreover, exponential PDP slope [4] can be observed since the underground parking lot is rather a closed cavity and the multiple reflections/scatterings, or diffraction may compose of the reverberation effect. Therefore, the reverberation time [4], [5] is calculated from PDP and shown in Table I. The reverberation time of an indoor channel, denoted as T_{rev}, is directly related to the PDP's exponential slope representing the decay rate by $T_{\text{rev}} = -\frac{10 \log_{10} e}{slope}$ [6] where *slope* has the unit of dB per second. Observation domain with fixed power range is applied to the PDP to calculate T_{rev}, and the range is determined visually by taking into account the effects of noise floor [4], [6]. It is observed that when Tx is at location 1 and Rx moves from location 1 to 11, there is a trend of the increase of T_{rev}, i.e. the decrease of the decay rate on PDP slope; at Rx location 12, the pillar 1 may serve as a diffraction scatterer; but at location 13-18, the pillar may serve as a obstructor, and a trend of the decrease of T_{rev} can be observed. When Tx is at location 2, and Rx moves from location S1 to S6, the trend of T_{rev} is to decrease, and the variations on T_{rev} is as large as 30 ns. Note that the calculation of T_{rev} excludes the effect of the LOS component or the strongest NLOS paths, and the large variations on T_{rev} indicate the large variation on the reverberation components. The reverberation components
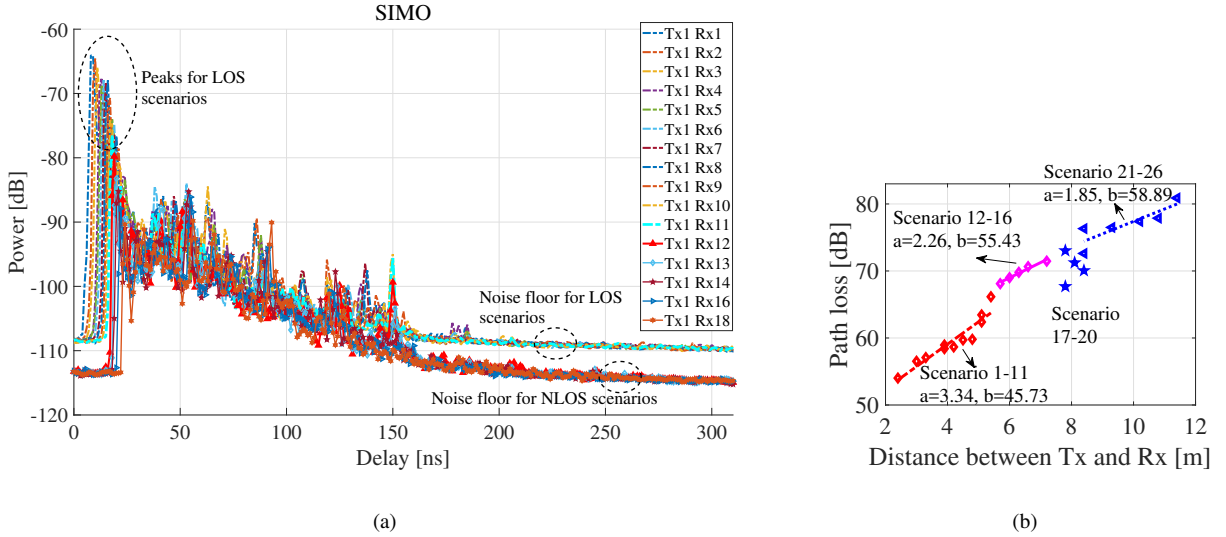
Fig. 2. (a) PDP of measured scenarios 1 - 16, (b) path loss models of measured scenarios

in scenario $21 \sim 26$ may result from the interaction of radio waves between car 1 and the two pillars, also may due to the interaction inside car 1 (front and rear windows of car 1 may allow radio waves go through). Moreover, it is interesting that the measured scenarios present a partially reverberant indoor environment, where T_{rev} in some locations stays similar and in some it varies a lot.

B. Path Loss

Path loss (PL) is the average attenuation of signals as radio waves propagate, and is calculated from the reciprocal of path gain (PG). PG is calculated by averaging the gains of local paths of all SIMO/SISO channels over entire bandwidth [7]

$$\text{PG} = \sum_{n_\tau = N_{\tau,\text{peak}}}^{N_{\tau,\text{max}}} \text{PDP}\left(n_\tau\right) \qquad (2)$$

where n_τ is the index of delay, $N_{\tau,\text{peak}}$ is the delay index for the first peak of PDP, $N_{\tau,\text{max}}$ is the maximum delay index at which the PDP power level is greater than the noise floor, and the noise floor can be defined in the same way as in [6]. The total antenna gains of Tx and Rx are excluded from PL, and the PL results are shown in Table I. Furthermore, the PL results are linearly fitted to the well-known power-law model, and the change of PL is plotted with the change of distance d between Tx and Rx (in case of obstructed LOS), or the summation of the distance from Tx to reference point and the distance from reference point to Rx (in case of NLOS)

$$\text{PL}\left(d\right) = a10\log_{10}\left(d\right) + b + X \qquad (3)$$

where a is the PL exponent, b is the PL at the reference distance of 1 m, and X is the random variable following log-normal distribution. Linear regression fitted models are shown in Fig. 2 (b). Value a is 3.34 for scenarios $1 \sim 11$, 2.26 for $12 \sim 16$, and 1.85 for $21 \sim 26$. a for scenarios $1 \sim 16$

is larger than the value reported in [2], and a for scenarios $21 \sim 26$ is similar as that in [2]. Note that since b is not the same for the shown subsections, the PL model is perceived as floating-intercept (FI) model and b is intercept value. It is interesting to observe the significant spatial diversity again, as has been observed through T_{rev}. In scenarios $21 \sim 26$, the whole body of car 1 contributes to the major scatterers, and the large PL may results from the shadowing effect by car 1; while in scenarios $1 \sim 16$, the pillar 1 contributes to the major scatterers.

C. Delay Spread

While the PDP is the squared magnitude of the impulse response averaged over the small-scale fading, the root mean square (RMS) delay spread is the second central moment of the PDP and provides a compact description of the delay dispersion of channel. The RMS delay spread, denoted as DS, is defined by

$$\text{DS} = \sqrt{\frac{\sum_{n_\tau = N_{\tau,\text{peak}}}^{N_{\tau,\text{max}}} \text{PDP}\left(n_\tau\right)\left(\tau_{n_\tau} - \tau_{\text{mean}}\right)^2}{\sum_{n_\tau = N_{\tau,\text{peak}}}^{N_{\tau,\text{max}}} \text{PDP}\left(n_\tau\right)} - } \qquad (4)$$

where

$$\tau_{\text{mean}} = \frac{\sum_{n_\tau = N_{\tau,\text{peak}}}^{N_{\tau,\text{max}}} \text{PDP}\left(n_\tau\right)\tau_{n_\tau}}{\sum_{n_\tau = N_{\tau,\text{peak}}}^{N_{\tau,\text{max}}} \text{PDP}\left(n_\tau\right)} \qquad (5)$$

is the mean delay. The delay spreads for measured scenarios are shown in Table I. DS is the indicator of the time dispersion and the spread of interacting scatterers; as can be seen from scenario $1 \sim 16$, with the increase of the distance between Tx and Rx and with the obstruction of pillar 1, the DS increases. Similar trend can be observed for scenario $21 \sim 26$. For scenario $17 \sim 20$ where Tx is at location 2, the involved scatterers when Rx locates at 17 and 18 appear to result in larger DS than that when Rx at 1 and 3. The variations on
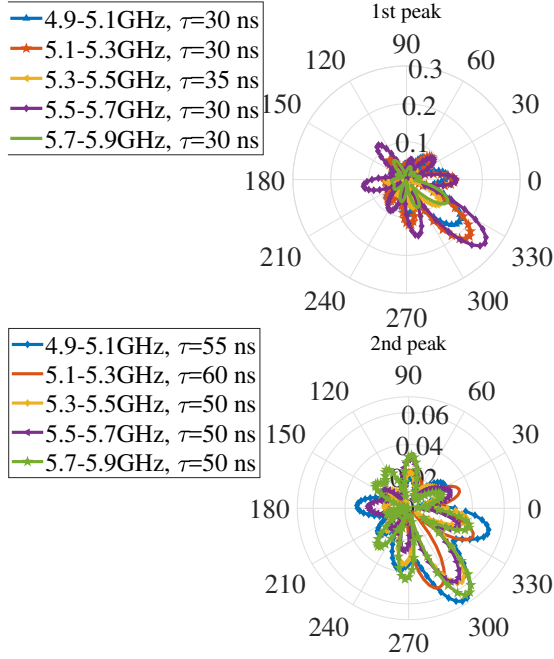
Fig. 3. Power angular spectrum of link Tx 2 and Rx 18

DS at different Tx and Rx locations again show that the interaction between radio waves and physical underground parking environment may has dramatic change even within several tenth meter square.

D. Coherence Bandwidth

The normalized frequency correlation function [7] under wide sense stationary (WSS) assumption is given by

$$\mathrm{C}(l) = \frac{1}{\sum_{n_\tau=0}^{N_f-1} \mathrm{PDP}\,(n_\tau)} \sum_{n_\tau=0}^{N_f-1} \mathrm{PDP}\,(n_\tau)\, e^{-j2\pi l n_\tau/N_f} \quad (6)$$

where $\mathrm{PDP}\,(n_\tau)$ is set to 0 for $n_\tau < N_{\tau,\mathrm{peak}}\,\&\,n_\tau > N_{\tau,\max}$, and $l = 0, 1, \ldots, N_f - 1$. The coherence bandwidth (CB) is determined at the correlation level of $C = 0.9$, and the results are shown in Table I. CB depends on the dominant propagation mechanism, e.g., mechanism of LOS and specular reflection are considered more correlated along frequency than diffuse scattering. It can be found that the trend of CB is in contrast with DS. For instance, for obstructed LOS scenarios when Tx1 and Rx are close, CB reaches as high as 29 MHz; as the Rx moves away from Tx1 and with the obstruction of pillar 1, CB drops.

E. Power Angular Delay Profile

Scenarios $1 \sim 20$ are measured with virtual circular array at Rx side. To avoid the delay difference among array elements in wideband channel with bandwidth of 1 GHz, the 1 GHz span is divided into 5 sub-bands each with 200 MHz bandwidth, and the joint power angular-delay profile (PADP) of SIMO radio channel for each sub-band is calculated by beamforming

toward the angle of arrival (AoA) $(\phi_{\mathrm{R}}, \theta_{\mathrm{R}})$ and the delay τ as [8]

$$P_{\mathrm{BF}}\,(\tau, \theta_{\mathrm{R}}, \phi_{\mathrm{R}}) =$$
$$\sum_{n_f=1}^{N'_f} \exp(-j2\pi f_{n_f}\tau) \boldsymbol{H}^\dagger\left(f_{n_f}\right) \boldsymbol{A}_{\mathrm{R}}\left(\phi_{\mathrm{R}}, \theta_{\mathrm{R}}, f_{n_f}\right) \quad (7)$$

where N'_f is the number of frequency points in each sub-band,

$$\boldsymbol{A}_{\mathrm{R}}\left(\phi_{\mathrm{R}}, \theta_{\mathrm{R}}, f_{n_f}\right) =$$
$$\left[A_{\mathrm{R},1}\left(\phi_{\mathrm{R}}, \theta_{\mathrm{R}}, f_{n_f}\right), \cdots, A_{\mathrm{R},N_{\mathrm{R}}}\left(\phi_{\mathrm{R}}, \theta_{\mathrm{R}}, f_{n_f}\right)\right]^T \in \mathbb{C}^{N_{\mathrm{R}} \times 1} \quad (8)$$

is the steering vector of Rx in AoA direction $(\phi_{\mathrm{R}}, \theta_{\mathrm{R}})$ at frequency f_{n_f},

$$A_{\mathrm{R},n_r}\left(\phi_{\mathrm{R}}, \theta_{\mathrm{R}}, f_{n_f}\right) = \exp\left(-j\frac{2\pi f_{n_f}}{c}\left(\hat{\boldsymbol{k}}_{\mathrm{R}} \cdot \bar{\boldsymbol{v}}_{\mathrm{R},n_r}\right)\right),$$
$$\hat{\boldsymbol{k}}_{\mathrm{R}} = -\left[\sin\left(\theta_{\mathrm{R}}\right)\cos\left(\phi_{\mathrm{R}}\right),\ \sin\left(\theta_{\mathrm{R}}\right)\sin\left(\phi_{\mathrm{R}}\right),\ \cos\left(\theta_{\mathrm{R}}\right)\right], \quad (9)$$

$\hat{\boldsymbol{k}}_{\mathrm{R}}$ is the unit vectors of propagation direction of impinging wave to Rx, and $\bar{\boldsymbol{v}}_{\mathrm{R},n_r}$ is the vector representing the position of n_r-th element of Rx array in local coordinate. $\{\cdot\}^T$ denotes the vector/matrix transpose, and $\{\cdot\}^\dagger$ denotes the conjugate transpose. Fig. 3 shows an example of the power azimuth-angle delay profile for the NLOS link of Tx 2 and Rx 18. The first delay peaks arriving at around 35 ns (corresponding to 10.5 m) at 5.3-5.5 GHz band and at 30 ns (9 m) for the rest. While the strongest power spectrum at 5.5-5.7 GHz sub-band comes from $\phi_{\mathrm{R}} = 321°$, that at 5.7-5.9 GHz comes from $\phi_{\mathrm{R}} = 330°$. These first delay peaks could probably due to the diffraction of pillar 2. For the second delay peaks appearing at around $50 \sim 60$ ns ($15 \sim 18$ m), the strongest power spectrum comes from direction $\phi_{\mathrm{R}} = 291°$ for 5.1-5.3 GHz band, and from $\phi_{\mathrm{R}} = 300° \sim 306°$ for the rest. These could be the reflected path from car 2 or from ceiling, after firstly be diffracted at pillar 2. This NLOS channel presents multipath richness due to the interaction of radio waves with vehicles, pillar, ceiling, etc.; it also gives us a hint that the localization of moving vehicles could probably be implemented through observing the variations on PADP of wideband multi-antenna radio channel.

IV. CONCLUSION

This paper reported the point-to-point wideband radio channel measurements and the channel characterizations in an underground parking lot. The measurements included both obstructed LOS and NLOS scenarios with the presence of commonly seen objects in underground parking at locations near link ends, such as vehicles, pillars, etc. The channel property parameters, including power angular profile, reverberation time, path loss, delay spread, coherence bandwidth, power angular delay profile were analyzed. It is found that: (1) the first PDP peak well indicates the distance between Tx and Rx in obstructed LOS scenario, or indicates the summation of the distance between Tx and reference point and that between

reference point and Rx; (2) the exponential slope at the "tail" of PDP was observed for all scenarios, and the observation on reverberation time indicates that the measured physical environment is more like a partially reverberant cavity in local vicinity of Tx and Rx; (3) the path loss exponent for obstructed LOS scenarios $1 \sim 11$ is 3.3, for NLOS scenarios $12 \sim 16$ is 2.3, for scenarios S1$\sim$S6 is 1.9, while the value reported in [2] is 1.5; (4) the delay spread and the coherence bandwidth present contrary trend and both show the spatial diversity in this partially reverberant parking lot corner; 5) the power angular-delay profile of the wideband SIMO channel indicates clearly the surrounding objects, and it appears promising to localize moving vehicles by using the variations on angular-delay power spectrum for future study.

REFERENCES

[1] B. Alavi, N. Alsindi, K. Pahlavan, "UWB Channel Measurements for Accurate Indoor Localization," in *Proc. 2006 IEEE Military Communications Conference (MILCOM),* Washington, DC, USA, Oct. 2006.

[2] J.Y. Lee, "UWB Channel Modeling in Roadway and Indoor Parking Environments," *IEEE Trans. Veh. Technol.,* vol. 59, no. 7, Sep. 2010.

[3] P. Kukolev, A. Chandra, T. Mikulasek, A. Prokes, "Out-of-Vehicle Time-of-Arrival Based Localization in Ultra-Wide Band," *International Journal of Distributed Sensor Networks,* vol. 12, no. 8, 2016.

[4] G. Steinbock, T. Pedersen, B.H. Fleury, W. Wang, R. Raulefs, "Experimental Validation of the Reverberation Effect in Room Electromagnetics," *IEEE Trans. Antennas Propag.*, vol. 63, no. 5, May 2015.

[5] J.B. Andersen, J.O. Nielsen, G.F. Pedersen, G. Bauch, and M. Herdin, "Room Electromagnetics," *IEEE Antennas and Propagation Magazine,* vol. 49, no. 2, pp. 2733, Apr. 2007.

[6] A. Bamba, W. Joseph, J.B. Andersen, E. Tanghe, G. Vermeeren, D. Plets, J.O. Nielsen, L. Martens, "Experimental assessment of specific absorption rate using room electromagnetics," *IEEE Trans. Electromagn. Compat.*, vol. 54, no. 4, Aug. 2012.

[7] M. Kim, Y. Konishi, Y. Chang, J. Takada, "Large Scale Parameters and Double-Directional Characterization of Indoor Wideband Radio Multipath Channels at 11 GHz," *IEEE Trans. Antennas Propag.,* vol. 62, no. 1, Jan. 2014.

[8] V. Kristem, S. Sangodoyin, C.U. Bas, M. Kaske, J. Lee, C. Schneider, G. Sommerkorn, C.J. Zhang, R.S. Thoma, A.F. Molisch, "3D MIMO Outdoor-to-Indoor Propagation Channel Measurement," *IEEE Trans. Wireless Communications,* vol. 16, no. 7, Jul. 2017.

[9] X. Cai, X. Yin, X. Cheng, A. Pérez Yuste, "An Empirical Random-Cluster Model for Subway Channels Based on Passive Measurements in UMTS," *IEEE Trans. on Communications,* vol. 64, no. 8, Aug. 2016.

[10] L. J. Greenstein, D. G. Michelson, V. Erceg. "Moment-method estimation of the Ricean K-factor," *IEEE Communications Letters,* vol. 3, no. 6, June. 1999.